

# Analysis and Dynamic Performance Improvement of Grid-Connected Voltage-Source Converters Under Unbalanced Network Conditions

Shahed Mortazavian, *Student Member, IEEE*, Masoud M. Shabestary, *Student Member, IEEE*, and Yasser Abdel-Rady I. Mohamed, *Senior Member, IEEE*

**Abstract**—The energy sector is moving toward an extensive utilization of distributed and renewable energy resources. Such resources are usually interfaced to power grids via voltage-source converters (VSCs). Due to the increased penetration level of VSC-interfaced resources, the utilization of interfacing VSCs to support host grids under unbalanced conditions (e.g., due to grid voltage unbalance, unbalanced load conditions and unsymmetrical faults) becomes essential. However, detailed dynamic analysis and systematic design procedure to enhance the dynamic performance of grid-connected VSCs equipped with grid-support controllers are not reported in the literature. To fill in this gap, this paper presents a detailed small-signal model and analysis of the dynamics of a grid-connected VSC equipped with the recently developed balanced positive-sequence control and positive/negative-sequence control methods to support the grid under unbalanced conditions. The effects of the short-circuit ratio, angle of the ac system impedance, and phase-locked-loop parameters on the transient behavior of the VSC are thoroughly studied and characterized. Furthermore, to improve the dynamic performance of grid-connected VSCs, a simple yet effective current-control-based compensator is developed to mitigate possible instabilities associated with the low-voltage operation. Comparative simulation and experimental results validate the theoretical analysis and the effectiveness of the proposed compensation scheme.

**Index Terms**—Grid-connected voltage-source converters (VSCs), grid-support, power converters, small-signal analysis, stability, state-space model, unbalanced grids.

## I. INTRODUCTION

NOWADAYS, distributed generation (DG) systems increasingly participate in the total energy production in power systems. Renewable energy resources such as wind turbines and photovoltaic systems are emerging to enhance the efficiency and safety of new grids and overcome the worldwide increasing power demand. Low-voltage ride-through (LVRT) has also recently become a mandatory requirement for the installation of DGs [1], [2]. According to the new grid codes, the grid-connected converters (GCCs) used in DG should withstand different grid faults [3]. Among hundreds of studies on

Manuscript received December 4, 2015; revised April 27, 2016; accepted August 18, 2016. Date of publication December 1, 2016; date of current version May 9, 2017. Recommended for publication by Associate Editor L. Zhang.

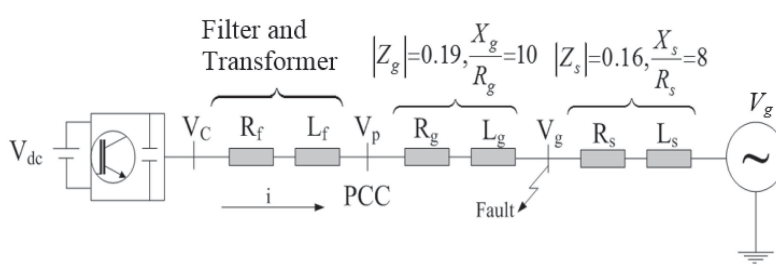
The authors are with the Department of Electrical and Computer Engineering, University of Alberta, Edmonton, AB T6G 2V4, Canada (e-mail: shahed1@ualberta.ca; masoud2@ualberta.ca; yasser\_rady@ieee.org).

Color versions of one or more of the figures in this paper are available online at <http://ieeexplore.ieee.org>.

Digital Object Identifier 10.1109/TPEL.2016.2633994

new grid codes and LVRT technologies in GCCs, some recent works have analyzed the stability of such systems [3]–[6]. In [7], some different reference current generation (RCG) methods are presented to comply with the power system LVRT requirements. In this paper, the balanced positive-sequence control (BPSC) and positive–negative-sequence compensation (PNSC) strategies are selected to be studied thoroughly using small-signal analysis. In fact, the study of the dynamic behavior of a GCC under unbalanced network condition using small-signal stability analysis with positive/negative voltage and current state variables has not yet been addressed in the literature. The small-signal stability analysis is based on the fact that the perturbations studied in the system are small in magnitude, in the sense that they do not excite significant nonlinear behaviors, thus allowing the nonlinear dynamics of the system to be represented by a linearized model, for studies around an equilibrium point. It is a simplification of the dynamic behavior providing general information to power engineers, which cannot be easily retrieved from nonlinear simulations and analyses [8]. The unbalanced condition can considerably affect the dynamic behavior of a GCC. Therefore, a full characterization of the unbalanced system is needed (e.g., such as the impacts of the phase-locked loop (PLL) parameters and different RCG strategies) to obtain an accurate assessment of the dynamic behavior of a GCC under unbalanced conditions.

Studies in [4] and [5] are based on the data analysis methods. The main drawback of these methods is that they need time-domain data of the system under study, and the observed dynamic response depends on the specifically analyzed perturbation, although they can be applied to any system by the use of nonlinear simulations [9]. Also, such methods mainly provide information on the modes of the system. Thus, some information, such as damping ratios and oscillation frequencies can only be estimated. If additional information regarding mode shapes and participation factor analysis (PFA) is needed, then a model-based analysis is necessary, and the system must be analyzed by its linearized model, normally represented in the state space [10], [11]. Because small-signal stability analysis is originally used in the large power transmission systems, several simplifications are often applied. Important among these is the consideration of a balanced three-phase system, which allows the power system to be represented by its single-phase equivalent [12], and the consideration of a phasor-domain model for



|   |                            |
|---|----------------------------|
| <i>DG Rating</i>  | 1.0 MVA, 480 V             |
| <i>V<sub>dc</sub></i>   | 1.2 kV                     |
| <i>C<sub>dc</sub></i>   | 120 $\mu$ F                |
| <i>R<sub>f</sub>, <i>L<sub>f</sub></i></i>  | 2 m $\Omega$ , 100 $\mu$ H |
| PI current control parameters ( <i>K<sub>p_init</sub></i> , <i>K<sub>i_init</sub></i> ) | 0.1, 2                     |
| System rated voltage:   | 27.6 kV                    |
| System rated power:   | 10 MVA (base power)        |
| System Short-Circuit Ratio (SCR):   | 6                          |

Fig. 1. Test system.

the analyzed power system. These simplifications are needed for the development of a linear model with a defined operating point [13].

In this paper, a state-space model of GCCs in dispatchable DG applications is presented for small-signal stability analysis under unbalanced and low-voltage conditions. Because power distribution systems are naturally unbalanced (due to their lines and loads characteristics, and increasing penetration of DG), such a tool is necessary to investigate a reliable and secure operation [14]. Therefore, the development of a *dq*-frame small-signal model is presented in this paper for the study of the dynamic performance of GCCs with different RCG techniques in unbalanced systems. The presented state-space model is then used to develop an improved compensation method. This compensator has enhanced the dynamic behavior of the GCC system under fault transients and low-voltage operation. The obtained analytical model presented in this paper is compared to the dynamic behavior observed from the nonlinear detailed time-domain simulations and also a scaled-down laboratory prototype. The results show the accuracy of the proposed state-space models.

This paper is organized as follows. Section II presents the studied system with a GCC and studied RCG strategies. The mathematical modeling of the studied system and applied controllers are also given in this section. The linearized state-space model of the GCC system is explained in Section III. Small-signal model validation and four test cases are presented and comparative results are shown in Section IV. Section V proposes an improved compensation method to enhance the transient performance of the system. The experimental results on a laboratory prototype are presented in Section VI. Finally, Section VII summarizes and concludes the paper.

## II. STUDIED POWER SYSTEM AND CONTROLLERS EQUATIONS

Fig. 1 shows a typical 1.0 MVA, 480 V converter-based DG system connected to a typical 27.6 kV medium-voltage distribution system via an interfacing filter and transformer with equivalent resistance and inductance  $R_f$  and  $L_f$ . The grid is modeled as Thevenin's equivalent circuit consisting of an equivalent resistance and inductance  $R_s$  and  $L_s$ , respectively. The line impedance between the source terminal and the point of common coupling (PCC) is  $Z_g$ .  $V_c$  is the voltage of the DG

terminal whereas  $V_p$  is the voltage at the PCC. Because the DG-side converter regulates the dc-link voltage, the dc-link voltage is considered constant in the study of GCCs. Such a system is widely used in studies related to LVRT and converter controls to support power grids under unbalanced condition [3], [14]–[16].

According to Fig. 1, the ac side dynamics of the interfacing converter system is as follows:

$$L_f \left( \frac{di}{dt} \right) = -R_f i + V_c - V_p \quad (1)$$

$$L_g \left( \frac{di}{dt} \right) = -R_g i + V_p - V_g. \quad (2)$$

### A. Balanced and Unbalanced System

In a balanced network, the voltage and current can be simply expressed in the positive-sequence *dq* reference frame as

$$L_f \frac{d}{dt} \begin{bmatrix} i_d \\ i_q \end{bmatrix} = -R_f \begin{bmatrix} i_d \\ i_q \end{bmatrix} + \begin{bmatrix} V_{cd} \\ V_{cq} \end{bmatrix} - \begin{bmatrix} V_{pd} \\ V_{pq} \end{bmatrix} - L_f \omega \begin{bmatrix} -i_q \\ i_d \end{bmatrix} \quad (3)$$

$$L_g \frac{d}{dt} \begin{bmatrix} i_d \\ i_q \end{bmatrix} = -R_g \begin{bmatrix} i_d \\ i_q \end{bmatrix} + \begin{bmatrix} V_{pd} \\ V_{pq} \end{bmatrix} - \begin{bmatrix} V_{gd} \\ V_{gq} \end{bmatrix} - L_g \omega \begin{bmatrix} -i_q \\ i_d \end{bmatrix}. \quad (4)$$

By neglecting the zero sequence components, a three-phase signal in an unbalanced network can be decomposed into the positive and negative sequence components [18]. The detailed description of the transformations from  $\alpha\beta$  to  $dq^+$  and  $dq^-$  frames can be found in [18]. Based on these transformations, the system equations can be expressed by (5)–(8) during unbalanced condition as follows:

$$L_f \frac{d}{dt} \begin{bmatrix} i_d^+ \\ i_q^+ \end{bmatrix} = -R_f \begin{bmatrix} i_d^+ \\ i_q^+ \end{bmatrix} + \begin{bmatrix} V_{cd}^+ \\ V_{cq}^+ \end{bmatrix} - \begin{bmatrix} V_{pd}^+ \\ V_{pq}^+ \end{bmatrix} - L_f \omega \begin{bmatrix} -i_q^+ \\ i_d^+ \end{bmatrix}, \quad (5)$$

$$L_f \frac{d}{dt} \begin{bmatrix} i_d^- \\ i_q^- \end{bmatrix} = -R_f \begin{bmatrix} i_d^- \\ i_q^- \end{bmatrix} + \begin{bmatrix} V_{cd}^- \\ V_{cq}^- \end{bmatrix} - \begin{bmatrix} V_{pd}^- \\ V_{pq}^- \end{bmatrix} + L_f \omega \begin{bmatrix} -i_q^- \\ i_d^- \end{bmatrix} \quad (6)$$

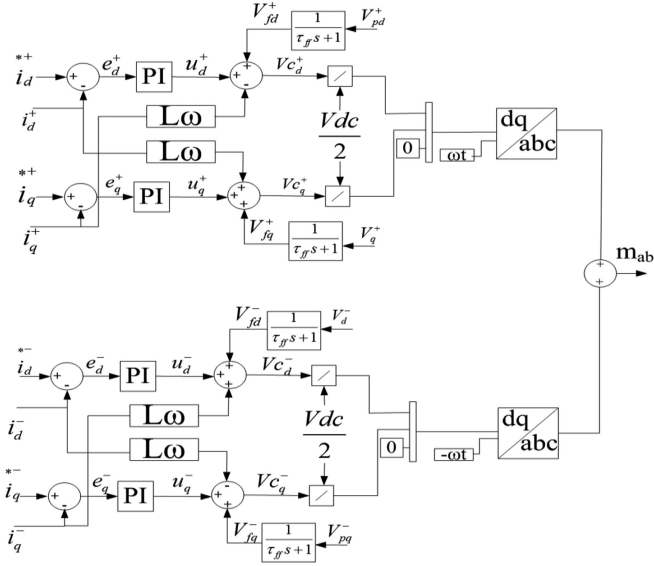


Fig. 2. Current controller block in positive and negative  $dq$  frames.

$$L_g \frac{d}{dt} \begin{bmatrix} i_d^- \\ i_q^- \end{bmatrix} = -R_g \begin{bmatrix} i_d^- \\ i_q^- \end{bmatrix} + \begin{bmatrix} V_{pd}^- \\ V_{pq}^- \end{bmatrix} - \begin{bmatrix} V_{gd}^- \\ V_{gq}^- \end{bmatrix} + L_g \omega \begin{bmatrix} -i_q^- \\ i_d^- \end{bmatrix} \quad (7)$$

$$L_g \frac{d}{dt} \begin{bmatrix} i_d^+ \\ i_q^+ \end{bmatrix} = -R_g \begin{bmatrix} i_d^+ \\ i_q^+ \end{bmatrix} + \begin{bmatrix} V_{pd}^+ \\ V_{pq}^+ \end{bmatrix} - \begin{bmatrix} V_{gd}^+ \\ V_{gq}^+ \end{bmatrix} - L_g \omega \begin{bmatrix} -i_q^+ \\ i_d^+ \end{bmatrix}. \quad (8)$$

In unbalanced conditions, there are four current components to be controlled as presented in (5)–(8), i.e.,  $i_d^+$ ,  $i_q^+$ ,  $i_d^-$ , and  $i_q^-$ . Therefore, the applied current control system consists of four independent proportional-integral (PI) controllers in the positive and negative  $dq$  frame, as shown in Fig. 2.

### B. Traditional RCG Techniques

In the first control technique, the reference current is generated using the following basic instantaneous power equations in the  $dq$  frame when the PLL is in the steady state and synchronized

$$P_s(t) = \frac{3}{2} V_{pd} i_d, \quad Q_s(t) = \frac{-3}{2} V_{pd} i_q. \quad (9)$$

Using feedback from the PCC voltage measurement ( $V_{pd}$  and  $V_{pq}$ ) to this controller,  $i_d^*$  and  $i_q^*$  are calculated as (10). This controller is called RCG strategy-1 (RCGS-1)

$$i_d^* = \frac{2}{3} \frac{P^*}{V_{pd}}, \quad i_q^* = \frac{-2}{3} \frac{Q^*}{V_{pd}}. \quad (10)$$

In the second strategy,  $i_d^*$  and  $i_q^*$  are generated using PI active power and voltage controllers as presented in [21]. This controller is called RCG strategy-2 (RCGS-2).

### C. Improved RCG Techniques for Grid Support

In this section, two newly proposed RCG strategies [7], [19]–[20] are presented. The selected strategies are the BPSC and

PNSC, and they are used to generate the inverter reference currents to deliver the reference active and reactive powers,  $P^*$  and  $Q^*$ .

The general reference currents  $i_p^*$  and  $i_q^*$  can be obtained using (11)

$$i_p^* = g v, \quad i_q^* = b v_\perp \quad i^* = i_p^* + i_q^* \quad (11)$$

where  $g$  and  $b$  can be considered as instantaneous conductance and susceptance [20]. For the BPSC strategy [19], the conductance and susceptance can be defined as

$$i_p^* = G^+ v^+, \quad G^+ = \frac{2/3 P^*}{|V^+|^2} \quad (12)$$

$$i_q^* = B^+ v_\perp^+, \quad B^+ = \frac{-2/3 Q^*}{|V^+|^2}. \quad (13)$$

Using (12) and (13), the reference currents only follow the positive sequence and become sinusoidal and balanced even under the unbalanced condition. The reference current equations in the positive and negative  $dq$  frames are

$$\begin{bmatrix} i_d^{+*} \\ i_q^{+*} \end{bmatrix} = \begin{bmatrix} i_{pd}^{+*} \\ i_{pq}^{+*} \end{bmatrix} + \begin{bmatrix} i_{Qd}^{+*} \\ i_{Qq}^{+*} \end{bmatrix} = G^+ \begin{bmatrix} V_d^+ \\ V_q^+ \end{bmatrix} + B^+ \begin{bmatrix} -V_q^+ \\ V_d^+ \end{bmatrix} \quad (14)$$

$$i_d^{-*} = i_q^{+*} = 0. \quad (15)$$

In the PNSC strategy, the reference-current contains a set of positive- and negative-sequence components and is designed to remove some oscillations from the instantaneous active/reactive powers [19]. Using these equations, the reference currents  $i_p^*$  and  $i_q^*$  can be obtained as

$$\begin{aligned} i_p^* &= i_p^{+*} + i_p^{-*} = G^+ V^+ + G^- V^-, \quad G^+ = -G^- \\ &= \frac{P^*}{|V^+|^2 - |V^-|^2} \end{aligned} \quad (16)$$

$$\begin{aligned} i_q^* &= i_Q^{+*} + i_Q^{-*} = B^+ V_\perp^+ + B^- V_\perp^-, \quad B^+ = -B^- \\ &= \frac{Q^*}{|V^+|^2 - |V^-|^2}. \end{aligned} \quad (17)$$

Then, the reference-current equations in the positive  $dq$  frame will be obtained similar to (14) and in the negative  $dq$  frames are expressed as

$$\begin{bmatrix} i_d^{-*} \\ i_q^{-*} \end{bmatrix} = \begin{bmatrix} i_{pd}^{-*} \\ i_{pq}^{-*} \end{bmatrix} + \begin{bmatrix} i_{Qd}^{-*} \\ i_{Qq}^{-*} \end{bmatrix} = G^- \begin{bmatrix} V_d^- \\ V_q^- \end{bmatrix} - B^- \begin{bmatrix} -V_q^- \\ V_d^- \end{bmatrix}. \quad (18)$$

In this paper, the BPSC and PNSC are selected as improved RCG techniques to be studied in the small-signal analysis and compared to the conventional GCC control strategies.

### III. STATE-SPACE MODEL

A linearized mathematical model of the studied power system (see Fig. 1) in the standard form of

$$\Delta \dot{\mathbf{X}} = A \Delta \mathbf{X} + B \Delta \mathbf{U} \quad (19)$$

TABLE I  
LIST OF STATE VARIABLES FOR FOUR STRATEGIES

| BPSC and PNSC   | RCGS-1  | RCGS-2   |
|---|---|--|
| $X = [i_d^+, i_q^+, i_d^-, i_q^-, \int e_d^+ dt, \int e_q^+ dt, \int e_d^- dt, \int e_q^- dt, \int \omega dt, \int v_q^+ dt, v_{fd}^+, v_{fq}^+, v_{fd}^-, v_{fq}^-]^T$ | $X = [i_d, i_q, \int e_d dt, \int e_q dt, \int \omega dt, \int v_q dt, v_{fd}, v_{fq}]^T$ | $X = [i_d, i_q, \int e_d dt, \int e_q dt, \int \omega dt, \int v_q dt, v_{fd}, v_{fq}, \int e_p dt]^T$ |

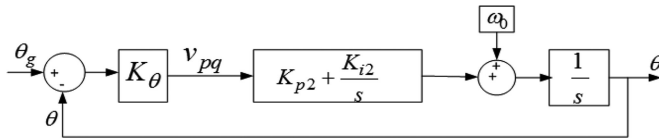


Fig. 3. PLL system.

is developed. This model is used to

- 1) design the controllers more accurately considering the system dynamics;
- 2) examine the system sensitivity to various control parameters variation;
- 3) analyze the system dynamics in GCC integration into power grids with different characteristics (particularly connection of a GCC to a weak grid);
- 4) investigate the effectiveness of the proposed compensation method.

The state variables for each strategy are given in Table I.

The input variable matrix in all methods is

$$u = [V_{gd}^+, V_{gq}^+, V_{gd}^-, V_{gq}^-]. \quad (20)$$

The linearized equations of controllers are divided into three parts:

- 1) PLL equations
- 2) current controller (CC) and PWM generator equations;
- 3) RCG equations.

The state variables  $\int \omega dt$ ,  $\int v_q^+ dt$  and  $\int v_q^- dt$  are obtained from the PLL equations. The other state variables are attained from the equations of the CCs and RCG strategies.

#### A. PLL Equations

The linear model of the utilized PLL system [17] is shown in Fig. 3.

Equation (21) represents the dynamics of the PLL controller where  $\omega$  is the angular frequency and  $\theta$  is the phase angle obtained from the PLL.  $\theta$  is synchronized to the PCC ac voltage

$$\theta = \int \omega dt, \quad \omega = \omega_0 + K_{p2}V_{pq} + K_{i2} \int V_{pq} dt. \quad (21)$$

However, in the positive and negative  $dq$  frames, the  $V_{pq}^+$  voltage is measured and fed into the PLL to synchronize  $\theta$ . Therefore, the linearized form of (21) in the new frame is

$$\Delta\theta = \int \Delta\omega dt, \quad \Delta\omega = K_{p2}\Delta V_{pq}^+ + K_{i2} \int \Delta V_{pq}^+ dt \quad (22)$$

where  $\Delta V_{pq}^+$  is obtained from the linearized form of (8).

#### B. CC and PWM Generator Equations

The equation sets of (3)–(4) and (5)–(8) are linearized to obtain the current state variables presented in Table I. The linearized equations of this part are all obtained based on the diagram shown in Fig. 2. The equations of the output voltage of the voltage-source converters (VSC) ( $V_c$ ) are derived as

$$\begin{aligned} \Delta V_{cd}^+ &= \Delta u_d^+ - L_f \omega_0 \Delta i_q^+ + \Delta V_{fd}^+, \\ \Delta V_{cq}^+ &= \Delta u_q^+ + L_f \omega_0 \Delta i_d^+ + \Delta V_{fq}^+, \\ \Delta V_{cd}^- &= \Delta u_d^- + L_f \omega_0 \Delta i_q^- + \Delta V_{fd}^-, \\ \Delta V_{cq}^- &= \Delta u_q^- - L_f \omega_0 \Delta i_d^- + \Delta V_{fq}^- \end{aligned} \quad (23)$$

in which  $\Delta u$  parameters are the output signals of the PI CCs in the positive and negative  $dq$  frames and  $\Delta V_f$ 's are the feed-forward signals passed through the low-pass filters [23]. The equations of  $\Delta u_d^+$  and  $\Delta V_{fd}^+$  are

$$\Delta u_d^+ = K_p \Delta e_d^+ + K_i \int \Delta e_d^+ dt \quad (24)$$

$$\Delta V_{fd}^+ = \frac{\Delta V_{pd}^+}{\tau_{ff}s + 1} \Rightarrow \Delta \dot{V}_{fd}^+ = \frac{1}{\tau_{ff}} (\Delta V_{pd}^+ - \Delta V_{fd}^+) \quad (25)$$

where  $K_p$  and  $K_i$  are the proportional and integral gains of the PI CCs.  $\Delta u$  and  $\Delta V_f$  in the other axes can be obtained similarly. Also,  $\Delta e$  in (24) represents the error between the reference and the measured currents and equals to  $\Delta e = i^* - i$  in each axis. The  $i^*$  variables are obtained from the RCG equations.

#### C. RCG Equations

Based on the selected RCG strategy to generate  $i^*$ , the linearized equations will be different. The linearized  $i^*$  equations for the BPSC and PNSC strategies are derived with details in the Appendix. The linearized  $i^*$  equations of RCGS-1 and RCGS-2 can be similarly derived.

#### IV. CASE STUDIES AND SIMULATION RESULTS

The simulation results for the four aforementioned control techniques are presented in Fig. 4. A single-phase-to-ground fault, between  $t = 0.4$  s and  $t = 0.6$  s, occurs and causes an unbalanced voltage. The grid voltage ( $V_g$ ) drops to zero during the fault, and no protection or tripping schemes are provided for the GCC in the simulations. As illustrated in Fig. 4, the BPSC is the only method that shows a balanced three-phase current during the fault. Moreover, high maximum phase currents, resulted by other three strategies, may cause a trip in the protection system and failure in successful fault ride through. In the case of

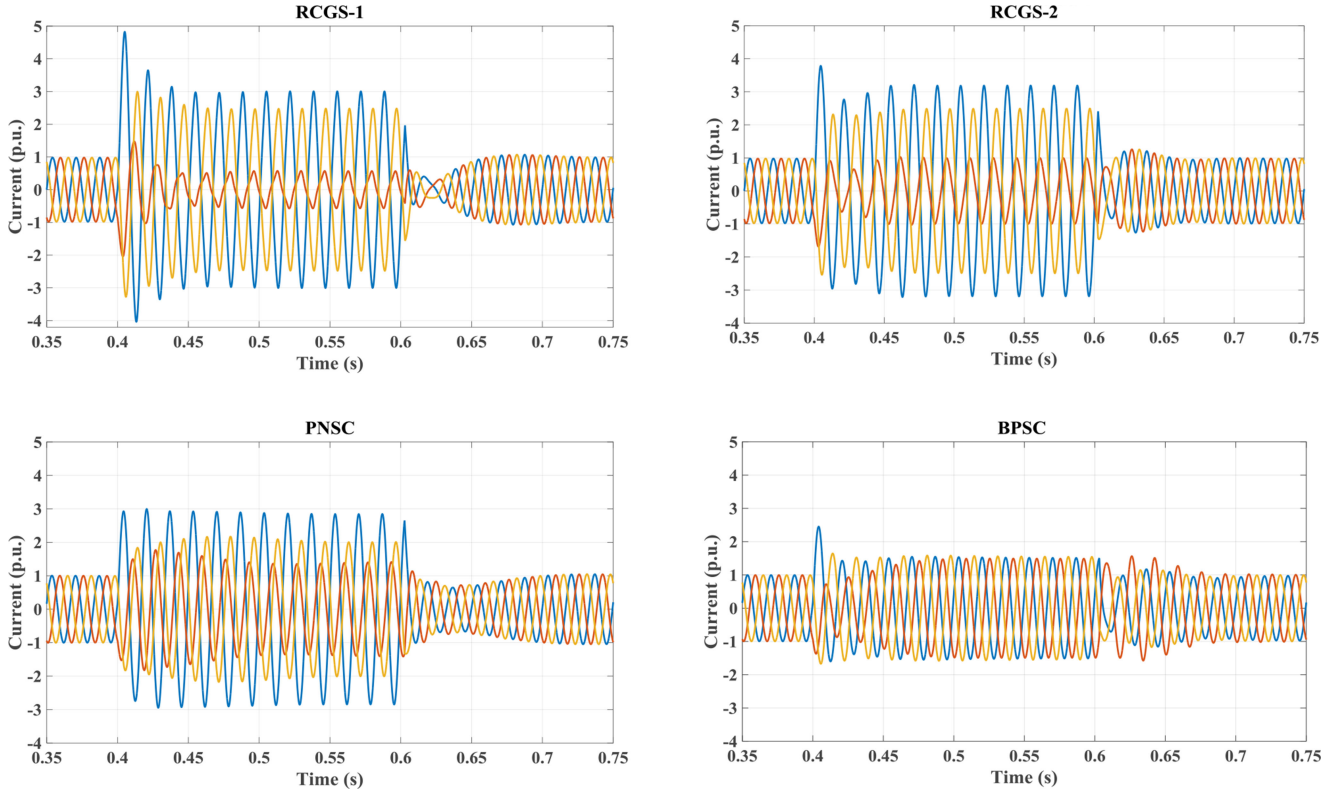


Fig. 4. Three-phase current results of the LVRT behavior with four RCG strategies.

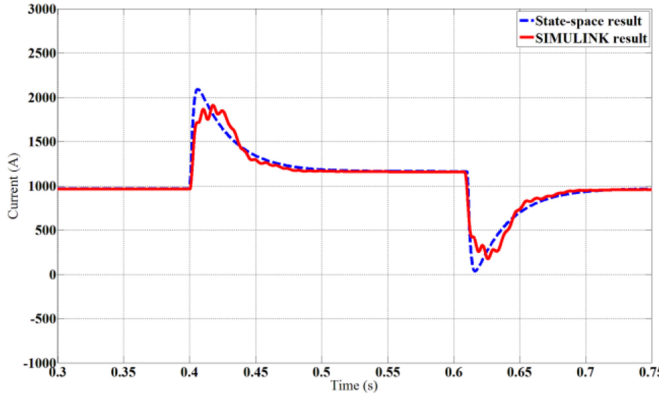


Fig. 5. Positive  $d$ -axis current for one-phase-to-ground fault between  $t = 0.4$  s to  $t = 0.6$  s.

1.0 p.u. active power delivery, the maximum phase current value, during the fault, is less than 1.5 p.u. for the BPSC strategy; but, in all other three methods, this value is around 3 p.u. The only problem in the BPSC results is the transient behavior of the GCC in the fault occurrence and clearance. The phase current values on fault occurrence in all methods are high (i.e., 4.7 p.u. for RCGS-1, 3.7 p.u. for RCGS-2, 3 p.u. for PNSC, and 2.5 p.u. for BPSC).

#### A. State-Space Model Validation

To show the validity of the obtained state-space models, the time-domain response of the state-space model with the BPSC strategy is compared to the time-domain response of the non-

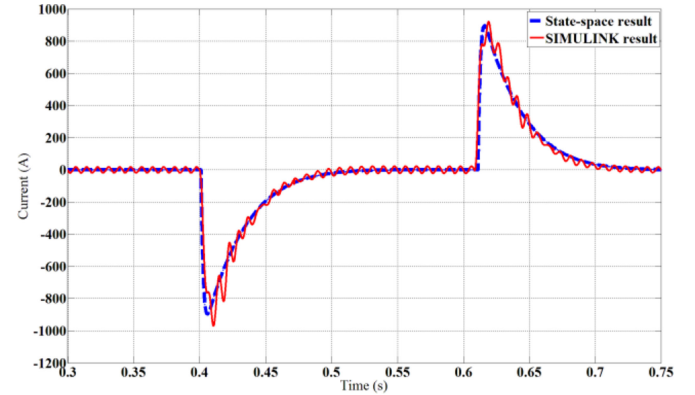


Fig. 6. Negative  $d$ -axis current for one-phase-to-ground fault between  $t = 0.4$  s to  $t = 0.61$  s.

linear model simulated in MATLAB-SIMULINK. Fig. 5 shows a comparison of the positive  $d$ -axis current of the detailed nonlinear model and that of the state-space model. In Fig. 6, the negative  $d$ -axis current results are also shown for the same case for a comparison between two models. Both figures show that the proposed state-space model is successfully accurate as the two traces are nearly identical.

#### B. Case Study 1: Small-Signal Stability Analysis of Systems With Different X/R Ratios

As presented in [21], the maximum power transfer by the GCC depends on the angle of the ac system impedance. Thus, the effect of the variation of the  $X/R$  ratio of the system on the

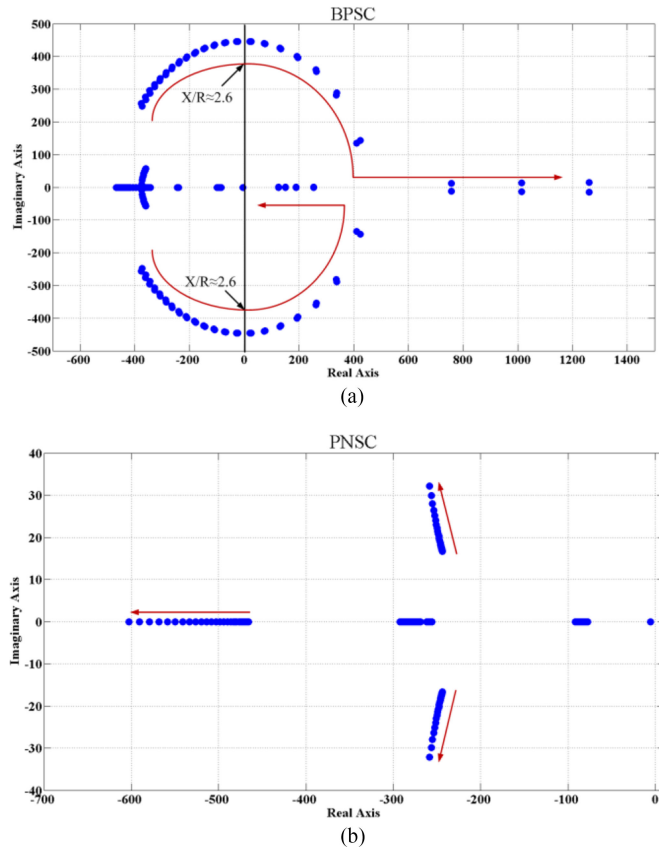


Fig. 7. Eigenvalue locus for  $X/R$  changes for (a) BPSC, (b) PNSC, SCR = 3.

performance of the presented strategies is studied in this case. The system short-circuit ratio (SCR) is almost constant during this case study.

The eigenvalues locus for  $X/R$  variation from 10 to 1 for the BPSC and PNSC strategies with SCR = 3 is shown in Fig. 7. As illustrated, the BPSC strategy is more sensitive to  $X/R$  changes, and it becomes unstable for  $X/R < 2.6$ . Repeating this test for a stronger system with SCR = 6 shows that the BPSC strategy remains stable even for  $X/R$  ratio of 1. Using the PNSC strategy, the system is stable when  $X/R$  changes from 10 to 1, for both SCR = 3 and SCR = 6. As shown in Fig. 7(b), the eigenvalue locus of the PNSC strategy for SCR = 3 presents negligible changes in poles. The same study for the other two conventional controllers (RCGS-1 and RCGS-2) shows that these approaches also remain stable for this range of  $X/R$  ratio changes with SCR = 3.

Therefore, in the case of low  $X/R$  ratio, the PNSC strategy and the conventional control methods will have more stable results in comparison to that of the BPSC in weaker grids ( $SCR \leq 3$ ) [22].

To verify the developed small-signal model, the simulation results of the nonlinear model, for a GCC with the BPSC strategy, are shown in Fig. 8. Fig. 8(a) and (b) demonstrates the GCC current in the  $dq^+$  axes for the cases of connection to weak ( $SCR = 3$ ) and strong ( $SCR = 6$ ) grids, respectively. These results show the effect of different system SCRs in the case of low

$X/R$  ratio (i.e.,  $X/R = 1$  for both cases). The results show instability in the case of the weak grid. However, the system is stable when connected to a strong grid with similar controller parameters. The simulation results of Fig. 8 verify the conclusions obtained from the linear models.

Additional studies reveal that the most dominant poles in the BPSC strategy that become unstable for  $X/R < 2$  are  $\lambda_{11}-\lambda_{14}$ . The PFA results for these eigenvalues are shown in Table II. It is indicated that these eigenvalues are mostly dependent on states  $x_3$ ,  $x_4$ ,  $x_7$ , and  $x_8$ , i.e.,  $i_d^-$ ,  $i_q^-$ ,  $\int e_d^- dt$ , and  $\int e_q^- dt$ . These parameters are shown in Fig. 2. As illustrated, all parameters affect  $V_c^-$ . In the BPSC strategy, the positive sequence voltage is forwarded to the current reference generator; therefore, it is controlled by the CC. Because the negative components of the PCC voltage are not forwarded to the controller, they are not controlled, and the system is highly affected by changing the  $X/R$  ratio. However, this problem does not show up in the PNSC strategy because both positive and negative components are controlled. Therefore, the system is not highly dependent on the  $X/R$  changes in the PNSC strategy.

The PFA for RCGS-1 shows that the effective poles when the  $X/R$  ratio changes depend on  $i_d$  and  $\int e_d dt$ , as presented in Table III. Because the negative and positive sequences are not controlled separately and because the effective parameter ( $i_d$ ) is controlled by the CC, the sensitivity of this control method to the grid strength is considerably less than that of the BPSC strategy, as presented in Fig. 7. Dominant poles of RCGS-2 show negligible variation with  $X/R$  changes.

### C. Case Study 2: Impact of the PLL Parameters and System SCR

It is shown in [21] that for low SCRs, the VSC performance is considerably affected by the PLL gains. However, a quantitative study is missing in the literature on GCCs performance with newly introduced RCG strategies under unbalanced and low-voltage conditions. Hence, an analytical study on the behavior of the GCC, with new RCG techniques under unbalanced and low-voltage conditions, is presented.

The eigenvalue locus for the PLL gain  $K_{p2}$  that changes from 0.1 to 10 (with the steps of 0.1) is plotted in Fig. 9. In these analyses, the operating point is  $P = 1.0$  p.u.,  $X/R = 9$  and  $K_{i2}$  is set to  $5^* K_{p2}$  for convenience in root locus plots [21]. As shown in Fig. 9, the BPSC and PNSC strategies are more sensitive to  $K_{p2}$  changes when SCR = 3; they become unstable from  $K_{p2} = 1.4$ . From now on, this value is called  $K_{p2\text{-threshold}}$ . However, other two conventional controllers are stable for this case until  $K_{p2\text{-threshold}} = 2.8$ . Therefore, in the case of using the BPSC or PNSC strategies, lower PLL gain selection is necessary to guarantee the system stability.

When a converter is connected to a weak grid, the dynamics of the control system and stability problems become more complicated. Besides, because the GCC controller parameters are often designed considering the connection to strong grids, in the case of a weak grid the performance of the GCC control system would become problematic. In Case Study 1, the effect of changing the  $X/R$  ratio on system poles is studied. In this

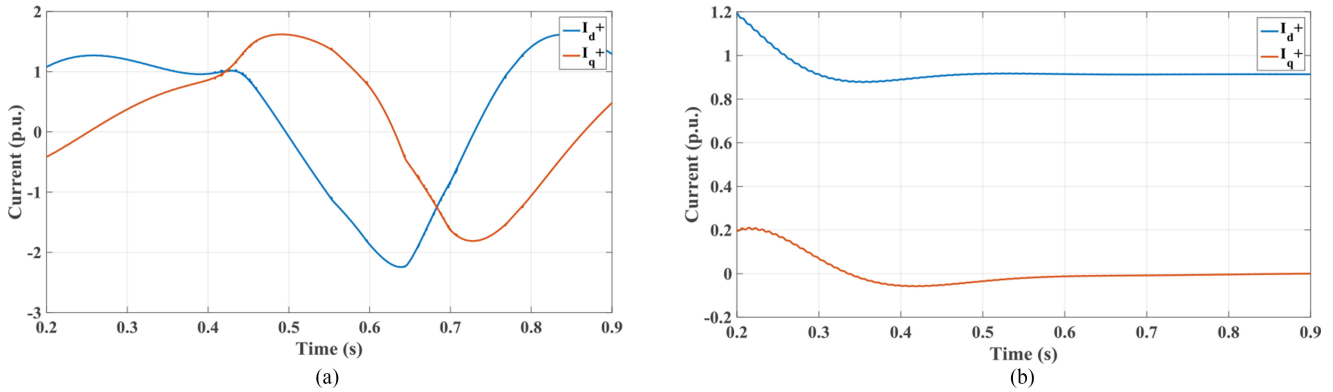


Fig. 8. Positive sequence current in the  $dq^+$  frame for different system SCRs and low  $X/R$  ratio in BPSC when  $X/R = 1$  and (a) SCR = 3, (b) SCR = 6.

TABLE II  
PFA ON THE MOST EFFECTIVE EIGENVALUES OF THE BPSC WHEN  $X/R$  CHANGES

|                   | $X_1$ | $X_2$ | $X_3$ | $X_4$ | $X_5$ | $X_6$ | $X_7$ | $X_8$ | $X_9$ | $X_{10}$ | $X_{11}$ | $X_{12}$ | $X_{13}$ | $X_{14}$ |
|-------------------|-------|-------|-------|-------|-------|-------|-------|-------|-------|----------|----------|----------|----------|----------|
| $\lambda_{11,12}$ | 0     | 0     | 0.245 | 0.245 | 0     | 0     | 0.24  | 0.24  | 0     | 0        | 0        | 0        | 0.009    | 0.009    |
| $\lambda_{13,14}$ | 0     | 0     | 0.25  | 0.25  | 0     | 0     | 0.25  | 0.25  | 0     | 0        | 0        | 0        | 0        | 0        |

TABLE III  
PFA ON RCGS-1 MOST EFFECTIVE EIGENVALUES WHEN  $X/R$  CHANGES

|                 | $X_1$ | $X_2$ | $X_3$ | $X_4$ | $X_5$ | $X_6$ | $X_7$ | $X_8$ |
|-----------------|-------|-------|-------|-------|-------|-------|-------|-------|
| $\lambda_{4,5}$ | 0.494 | 0     | 0.483 | 0.011 | 0.005 | 0     | 0     | 0.005 |

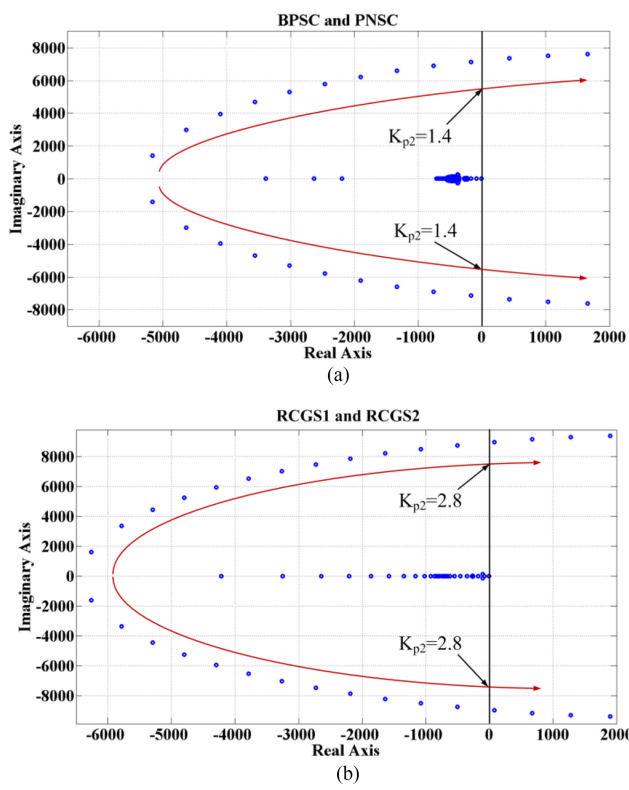


Fig. 9. Eigenvalue locus for PLL gains changes for (a) BPSC and PNSC, (b) RCGS1 and RCGS-2; when SCR = 3.

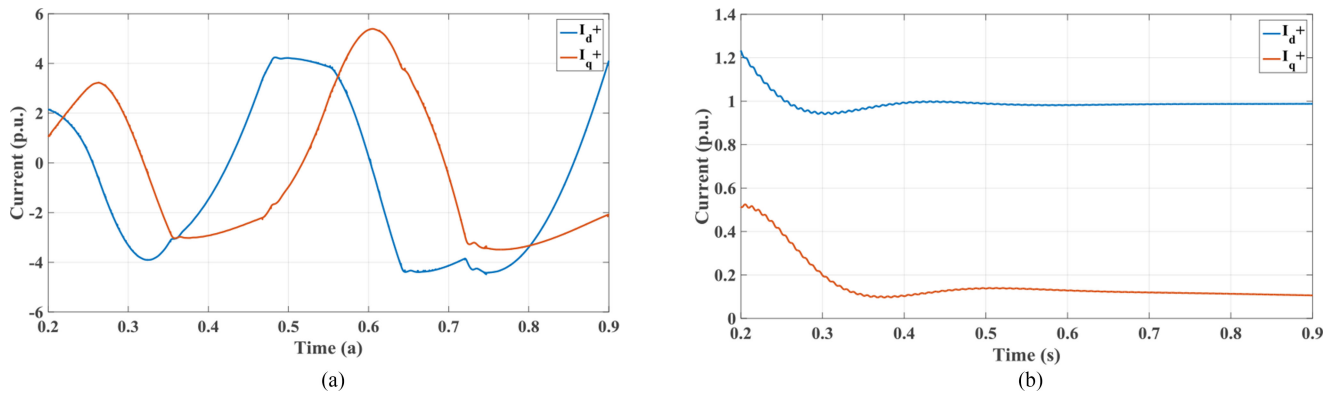
TABLE IV  
PLL PARAMETER CHANGE RESULTS

| SCR | $K_{p2}$ -threshold in BPSC and PNSC | $K_{p2}$ -threshold in RCGS-1 and RCGS-2 |
|-----|--------------------------------------|--|
| 1.3 | unstable for all $K_{p2}$            | 0.9                                      |
| 2.2 | 0.4                                  | 1.9                                      |
| 3   | 1.4                                  | 2.8                                      |
| 6   | stable for all $K_{p2}$              | stable for all $K_{p2}$                  |

case, the value of the system SCR is changed whereas the  $X/R$  ratio is fixed on 10, and its effect on the system stability with different RCG methods is studied. Table IV presents the results of the small-signal analysis of four strategies with different system SCRs. It is observed that the improved RCG strategies are also more sensitive to the system SCR, i.e., they are unstable for very weak grids (SCR = 1.3) even for very low  $K_{p2}$  values.

The simulation results of the nonlinear model for a GCC with the BPSC strategy is presented in Fig. 10. The results show instability in the case of connection to a weak grid. However, the system is stable when connected to a strong grid with similar controller parameters. The value of  $K_{p2}$  is 2 in both cases. The results verify the conclusions obtained from the small-signal analysis considering the effect of power system strength in designing the PLL control parameter.

Applying the PFA on these controllers for  $K_{p2} = 1$  and SCR = 3 shows that the sensitive poles for the BPSC and PNSC are  $\lambda_2$  and  $\lambda_3$  that are mostly dependent on  $x_2$ ,  $x_9$  and  $x_{12}$  as presented in Table V.  $x_2$ ,  $x_9$  and  $x_{12}$  are dependent on  $i_q^+$ ,  $\int \omega dt$  and  $V_{f,q}^+$ , respectively.  $V_{f,q}^+$  is the filtered feedforward signal from  $V_{pq}^+$  that is fed into PLL as the control signal.  $V_{pq}^+$  contributes to controlling  $\omega$ .  $i_q^+$  is also affected by  $V_{pq}^+$  as shown in (5). Therefore, it is reasonable for these poles to vary by changing  $K_{p2}$ .

Fig. 10. Positive sequence current in  $dq^+$  frame for BPSC when  $K_{p2} = 2$  and (a) SCR = 3, (b) SCR = 6.TABLE V  
PFA ON THE BPSC AND PNSC FOR PLL GAINS CHANGES

|      | $X_1$           | $X_2$ | $X_3$ | $X_4$ | $X_5$ | $X_6$ | $X_7$ | $X_8$ | $X_9$ | $X_{10}$ | $X_{11}$ | $X_{12}$ | $X_{13}$ | $X_{14}$ |   |
|------|-----------------|-------|-------|-------|-------|-------|-------|-------|-------|----------|----------|----------|----------|----------|---|
| BPSC | $\lambda_{2,3}$ | 0     | 0.198 | 0     | 0     | 0     | 0.036 | 0     | 0     | 0.306    | 0        | 0        | 0.459    | 0        | 0 |
| PNSC | $\lambda_{2,3}$ | 0.008 | 0.194 | 0     | 0     | 0     | 0.035 | 0     | 0     | 0.309    | 0        | 0        | 0.451    | 0        | 0 |

TABLE VI  
PFA ON RCGS-1 FOR PLL GAINS CHANGES

|             | $X_1$ | $X_2$ | $X_3$ | $X_4$ | $X_5$ | $X_6$ | $X_7$ | $X_8$ |
|-------------|-------|-------|-------|-------|-------|-------|-------|-------|
| $\lambda_2$ | 0     | 0.033 | 0     | 0     | 0.228 | 0     | 0     | 0.738 |
| $\lambda_3$ | 0     | 0.038 | 0     | 0     | 0.700 | 0     | 0     | 0.261 |

The same study for RCGS-1 and RCGS-2 shows that the most sensitive poles to the PLL parameters are  $\lambda_2$  and  $\lambda_3$  that depend on  $\int \omega dt$  (i.e.,  $x_5$ ) and  $V_{f,q}$  (i.e.,  $x_8$ ). The results for RCGS-1 are presented in Table VI. Therefore, changing the PLL parameters in all methods affect the dominant poles that are highly connected with PLL signals. Therefore, taking into account the results of Table IV will help in keeping the system stable for different SCRs.

#### D. Case Study 3: Damping Ratio of Dominant Poles

The damping ratio,  $\xi$ , represents the rate of decay in the amplitude of oscillations. For an oscillatory mode denoted by a complex eigenvalue  $\sigma \pm j\omega$ , the damping ratio is defined as

$$\xi = \frac{-\sigma}{\sqrt{\sigma^2 + \omega^2}}. \quad (26)$$

Considering the damping ratio for the dominant poles of the studied strategies, Fig. 11 shows the results for the BPSC strategy. As presented, for the system with SCR = 2.2, the PLL control parameter ( $K_{p2}$ ) should be less than 0.4 to have  $\xi > 0$ . Also, in this case,  $\xi$  starts to decay from the beginning (i.e.,  $K_{p2} = 0.1$ ) which represents an oscillatory behavior. However, for the system with SCR = 3, the selected  $K_{p2}$  can be

larger, and  $\xi$  starts to decrease from  $K_{p2} = 0.3$ , which shows a nonoscillatory behavior for this mode before  $K_{p2} = 0.3$ . For a stronger grid with SCR = 6, there is a negligible change in  $\xi$  and it stays almost constant at 1. The same trends are observed for  $\xi$  in the PNSC strategy while changing  $K_{p2}$ . These results also confirm the results obtained in case study 2 for the PLL parameters change.

Considering  $\xi$  when  $X/R$  changes, the results of Figs. 12 and 13 are obtained for the BPSC and PSNC strategies, respectively. For the BPSC, by increasing  $X/R$ , the damping ratio is also increased. Therefore, the system shows lower stability with lower  $X/R$  values.

For the PNSC strategy, Fig. 13 reveals that for both SCR values,  $\xi$  remains almost constant close to 1. The minor changes show that increasing  $X/R$  results in a higher  $\xi$ . These results again show the lower sensitivity to  $X/R$  changes in the PNSC in comparison to the BPSC strategy.

#### E. Case Study 4: Maximum Phase Current of Four Strategies

Conventional controllers showed higher stability in the case of weak grids. However, one of the most important characteristics of RCG techniques, during the fault, is the maximum phase current value ( $I_{\max}$ ) which affects the protection tripping and LVRT failure. Therefore, in this case, the  $I_{\max}$  characteristic during the fault is studied.

As presented in [19], the expressions of the  $I_{\max}$  for the BPSC and PNSC strategies are as follows:

$$I_{\max, \text{BPSC}} = \frac{P^2 + Q^2}{V_{p+}^2} \quad (27)$$

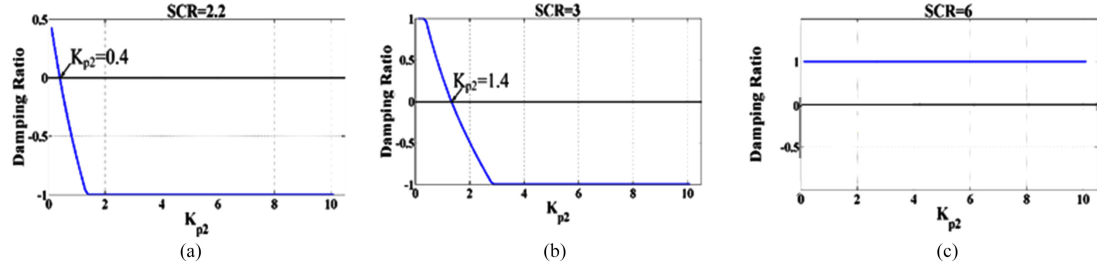


Fig. 11. Damping ratio versus  $K_{p2}$  of BPSC for (a) SCR = 2.2, (b) SCR = 3, and (c) SCR = 6.

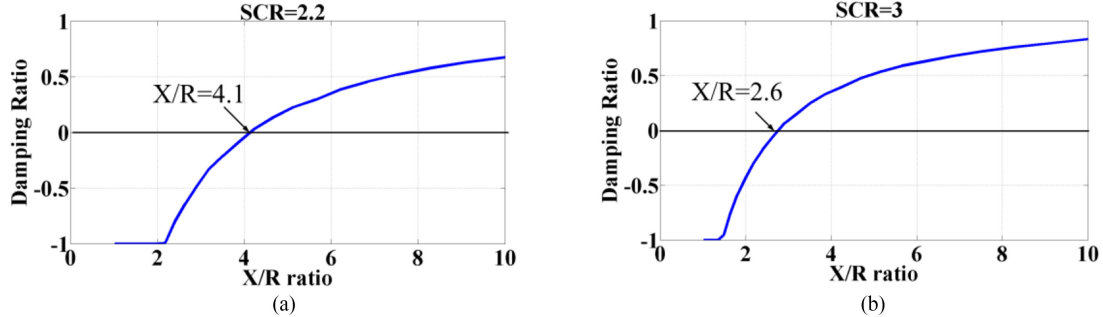


Fig. 12. Damping ratio versus  $X/R$  of BPSC for (a) SCR = 2.2, (b) SCR = 3.

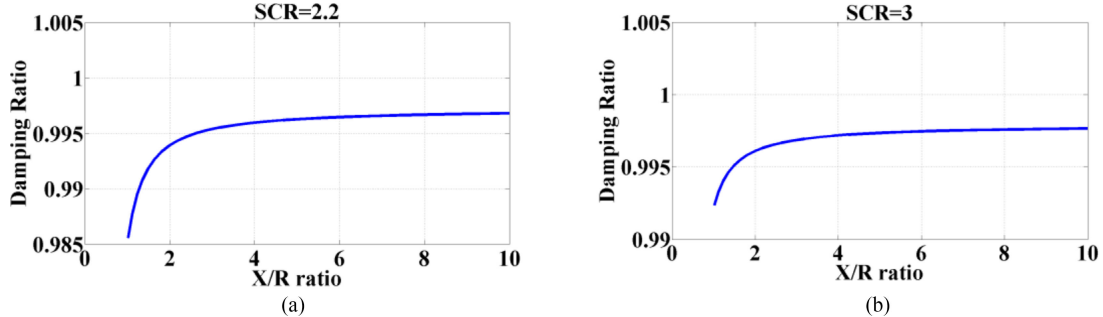


Fig. 13. Damping ratio versus  $X/R$  of PNSC for (a) SCR = 2.2, (b) SCR = 3.

$$I_{\max, PNSC} = \begin{bmatrix} \frac{P^2(V_2)^2 + Q^2(V_1)^2}{(V_{p+}^2 - V_{p-}^2)^2} \\ \frac{(V_2)^2 \left[ \frac{1}{2}P + \frac{\sqrt{3}}{2}Q \right]^2 + (V_1)^2 \left[ \frac{1}{2}Q + \frac{\sqrt{3}}{2}P \right]^2}{(V_{p+}^2 - V_{p-}^2)^2} \\ \frac{(V_2)^2 \left[ \frac{1}{2}P - \frac{\sqrt{3}}{2}Q \right]^2 + (V_1)^2 \left[ \frac{1}{2}Q - \frac{\sqrt{3}}{2}P \right]^2}{(V_{p+}^2 - V_{p-}^2)^2} \end{bmatrix} \quad (28)$$

where  $V_{p+}$  and  $V_{p-}$  stand for the positive and negative components of the PCC voltage, respectively, and,  $V_1$  and  $V_2$  are as follows:

$$V_1 = V_{p+} - V_{p-}, \quad V_2 = V_{p+} + V_{p-}. \quad (29)$$

The  $I_{\max}$  expression for RCGS-1 is as follows:

$$I_{\max, RCG1} = \frac{\frac{2}{3}P^*}{V_1}. \quad (30)$$

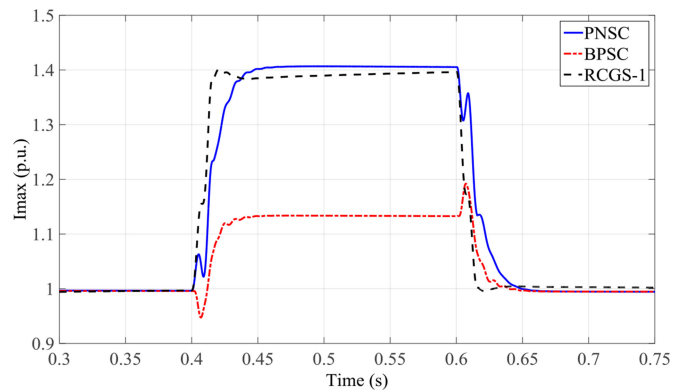


Fig. 14.  $I_{\max}$  for different RCG strategies.

Fig. 14 illustrates the  $I_{\max}$  values for these three RCG methods when SCR = 6. As presented, the BPSC strategy has a considerable lower  $I_{\max}$  value during the fault in comparison to the PNSC and RCGS-1. The maximum phase current value in the BPSC strategy is 1.19 p.u. whereas this value is 1.4 p.u. for the PNSC and RCGS-1. Therefore, although the BPSC is

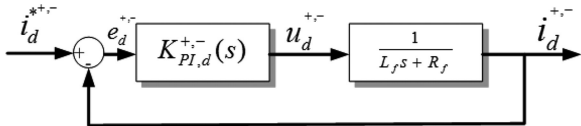


Fig. 15. Block diagram of the current-controlled VSC system in the  $d+-$  channel.

more susceptible to instability in weak grids when compared to the PNSC and the conventional controllers, it is a reliable strategy to be chosen in the case of severe faults. This is because the BPSC method yields a lower  $I_{\max}$  and decreases the chance of tripping of protection devices during the fault.

## V. PROPOSED COMPENSATION METHOD TO IMPROVE THE TRANSIENT BEHAVIOR

In this section, an improved CC design is proposed using the obtained state-space model to improve the transient performance and reduce the maximum phase current during fault occurrence and clearance. Typically, the design of the CC in the  $dq$  frame is based on considering the closed-loop CC as a first-order low-pass filter with unity gain and the time constant of  $\tau_i$  as  $G_i(s) = \frac{1}{\tau_i s + 1}$  [23]. The simplified block diagram of the current-controlled VSC system in the positive and negative  $d$ -axis is shown in Fig. 15. The same block diagram applies for the positive and negative  $q$ -axis. It is observed that the plant pole at  $s = -\frac{R_f}{L_f}$  is quite close to the origin. Therefore, in designing the compensator ( $K_{PI}(s)$ ), a zero is set to  $s = -\frac{K_i}{K_p}$  to cancel the plant pole. Besides, the loop gain is assumed to be  $s = \frac{K_p}{L_f}$  to provide the mentioned  $G_i(s)$  for the closed-loop transfer function. Therefore, in the traditional method, the values of  $K_p$  and  $K_i$  in the PI controller are selected as  $K_p = \frac{L_f}{\tau_i}$ ,  $K_i = \frac{R_f}{\tau_i}$ .

However, as shown in Section IV, using the CC designed with this method presents high maximum phase current in transients (see Fig. 4). To solve this problem, a new CC design method is proposed in this paper. In the proposed method, the parameters of four PI controllers, in the  $dq + -$  frame, are determined based on the eigenvalue analysis on the obtained state-space model. To find the proper values of  $K_p$  and  $K_i$ , the eigenvalue locus of the system poles are studied in the following steps. First, the value of  $K_p$  is kept constant (i.e.,  $K_p = \frac{L_f}{\tau_i}$ ) whereas the value of  $K_i$  is changed with a coefficient ( $\alpha$ ) from 0.1 to 10. As presented in Fig. 16(a), increasing the value of  $K_i$  moves the dominant poles toward the left half plane which provides a more stable system. However, four farther poles have moved toward the right, and their imaginary part is also increased. Therefore, based on (26), the damping ratio ( $\xi$ ) of these poles are decreased which can result in even higher overshoots in the BPSC strategy.

In the next step, the value of  $K_i$  is kept constant  $K_i = \frac{R_f}{\tau_i}$  and the value of  $K_p$  is increased with the same coefficient. The result in Fig. 16(b) demonstrates that the dominant poles move toward the right half plane which is not desirable. On the other hand, the imaginary part of the four farther poles is

decreasing faster. The desirable point about this case is that the imaginary parts of two of these poles decrease to zero which represent  $\xi \geq 1$ .

To obtain satisfactory results, it is proposed to combine the steps mentioned above. First, the  $\alpha$  coefficient of  $K_i$  is kept fixed at a selected value; then, both  $K_i$  and  $K_p$  are simultaneously changed with a similar coefficient ( $g$ ) changing from 0.1 to 4 (i.e.,  $K_i = g \times \alpha \frac{R_f}{\tau_i}$ ,  $K_p = g \frac{L_f}{\tau_i}$ ). The results for three different  $\alpha$  values are shown in Fig. 17. It is observed that as  $\alpha$  increases, the most dominant poles move farther from the origin. The value of  $\alpha = 5$  is selected here because it has moved the dominant poles of the system far enough from the origin representing a satisfactory stability.

The eigenvalue locus of the complete system poles are shown in Fig. 18 for  $\alpha = 5$  and  $g$  changing from 0.1 to 4. In this case, in addition to the movement of the most dominant poles toward the left [see Fig. 17(c)], the farther poles (representing the higher natural frequencies of the system) also move toward the left, as shown in Fig. 18. This results in a higher damping ratio of the faster poles which solves the high overshoot problem.

The damping ratio changes of the demonstrated poles of Fig. 18 ( $P_1$  to  $P_4$ ) are presented in Fig. 19. The value of  $\xi$ , which is obtained from (26), is increased and for  $g > 1.5$ , two poles ( $P_1$ ,  $P_2$ ) represent overdamped behavior and the other two ( $P_3$ ,  $P_4$ ) show high damping ratio close to 1. Therefore, shifting  $P_1$ – $P_4$  to the left by increasing the value of  $g$ , decreases the maximum overshoot.

However, increasing the value of  $g$  is also restricted because of the limitation on the time constant of the CC ( $\tau_i$ ). This time constant should be chosen enough smaller than the switching time of the switches (i.e.,  $\frac{1}{\tau_i} < 0.2\omega_{sw}$  [24] in which  $\omega_{sw}$  is the angular switching frequency). Assuming a reasonable value for the VSC switching frequency of 5 kHz [23], the value of  $\frac{1}{\tau_i}$  should be smaller than  $6.28 \times 10^3$ . Therefore, the value of the undamped natural frequency of the CC system ( $\omega_n$ ) should satisfy  $\omega_n = \frac{2}{3}(\frac{1}{\tau_i}) < \frac{2}{3}(0.2\omega_{sw})$  [23].  $\omega_n$  represents the distance of each pole from the origin.  $P_1$  has the maximum  $\omega_n$  when  $g$  is increased. Therefore, the limitation, on increasing the value of  $g$ , is to keep the real part of  $P_1$  lower than 4000. By choosing  $g = 3$ , this limitation is satisfied.

The simulation results of the positive sequence current in the  $dq$  frame for the BPSC strategy are shown in Fig. 20. Fig. 20(a) illustrates the cases for two different  $g$  values whereas  $\alpha = 5$ . It is demonstrated that with  $g = 3$ , the maximum overshoot value is considerably decreased in both fault occurrence and clearance incidents. It verifies the results obtained from eigenvalue analysis and Fig. 19. In Fig. 20(b), the same signals are shown for different  $\alpha$  values whereas  $g = 3$ . For the case of  $\alpha = 5$ , the transient oscillations are damped quickly and the settling time is remarkably improved. Therefore, a reasonable and effective choice for controller parameters can be  $K_p = 3 \times \frac{L_f}{\tau_i}$ ,  $K_i = 3 \times \frac{5 \times R_f}{\tau_i}$  (i.e.,  $\alpha = 5$  and  $g = 3$ ). Fig. 21 reveals the improved results of applying the proposed CC. As presented, the high overshoot of phase current on the fault occurrence is removed. It prevents any

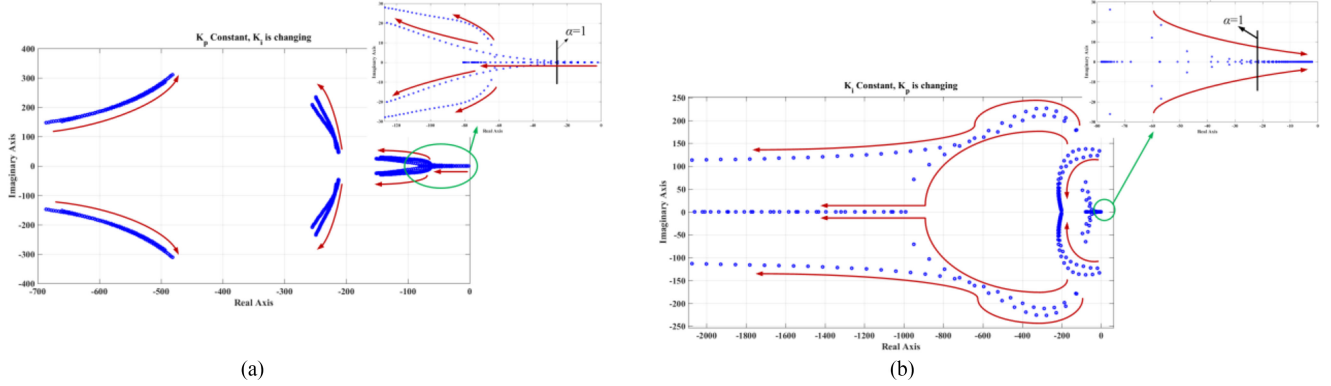


Fig. 16. Eigenvalue locus of changing (a) only  $K_i$ , and then (b)  $K_p$ , in BPSC strategy.

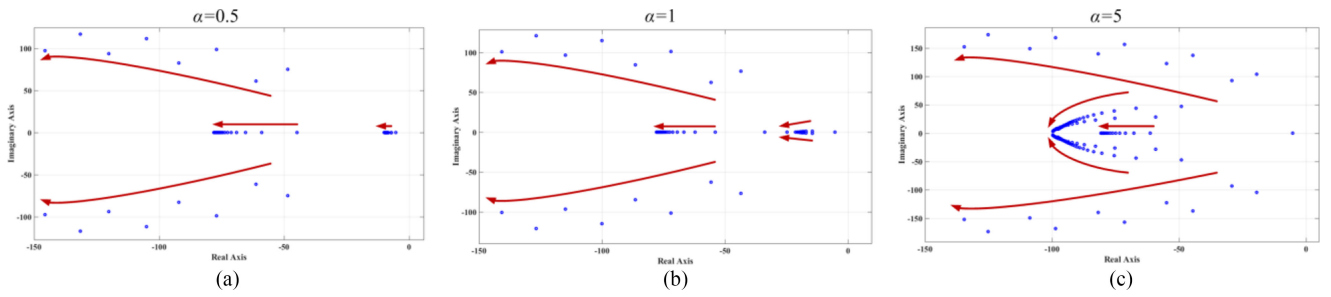


Fig. 17. Eigenvalue locus for most dominant poles when (a)  $\alpha = 0.5$ , (b)  $\alpha = 1$  and, (c)  $\alpha = 5$ .

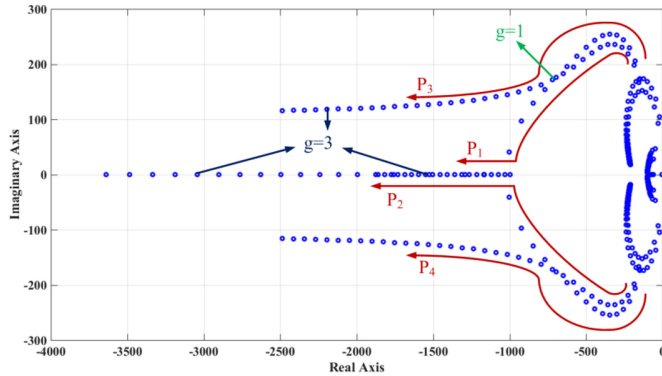


Fig. 18. Eigenvalue locus of the complete system poles when  $\alpha = 5$ .

potential undesired tripping in the system. Besides, the system represents a considerably faster response on both fault occurrence and clearance.

## VI. EXPERIMENTAL RESULTS

The improved and traditional RCG strategies are validated using a scaled down 1.0 kVA laboratory prototype as shown in Fig. 22. The key components for the laboratory setup are a dSPACE DS1104 real-time control system, three-leg VSC (a Semistack intelligent power module, which includes gate drives, six insulated gate bipolar transistors, and protection circuit), 60-Hz three-phase grid, interfacing transformer, and a sensor box to sample the voltage and current of the PCC. The VSC

inductor currents are measured by HASS-50-S current sensors whereas the voltages are measured by LEM-V-25-400 voltage sensors. The ac filter inductance and resistance are 1.20 mH and 0.06  $\Omega$ , respectively. The dc-link capacitance is 2.04 mF. The dSPACE1104 interfacing board is equipped with eight digital-to-analog channels and eight analog-to-digital channels to interface the measured signals to/from the control system. The software code is generated by the real-time-WorkShop under the MATLAB/Simulink environment. The grid stiffness is changed by connecting series inductors to the ac grid so that SCR at the PCC can be varied.

### A. System Performance With the Proposed Compensator

The performance of the system with the BPSC RCG method is investigated in the experimental setup using both traditional and the compensated CCs, proposed in Section V. The system experiences a single-phase-to-ground fault for 4 s. The compensation coefficients are chosen as  $g = 1$  and  $\alpha = 2$  to prevent high current transients. As shown in Fig. 23, both the magnitude and oscillations of the converter current in both fault occurrence and fault clearance are reduced using the proposed compensation method. Therefore, the experimental results also reveal the capability of the proposed compensation method in enhancing the system performance under unbalanced fault conditions.

### B. System Performance Under Different PLL Parameters

It is shown in Section IV-C that the system stability is higher when lower PLL parameters ( $K_{p2}$  and  $K_{i2}$ ) are chosen. In this

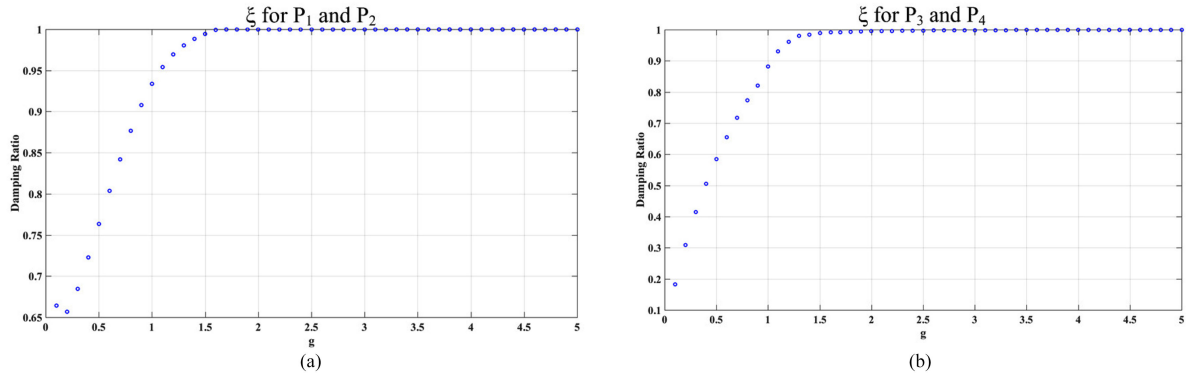


Fig. 19. Damping ratio versus  $g$  coefficient for the fastest poles (a)  $P_1$ ,  $P_2$ , (b)  $P_3$ ,  $P_4$ .

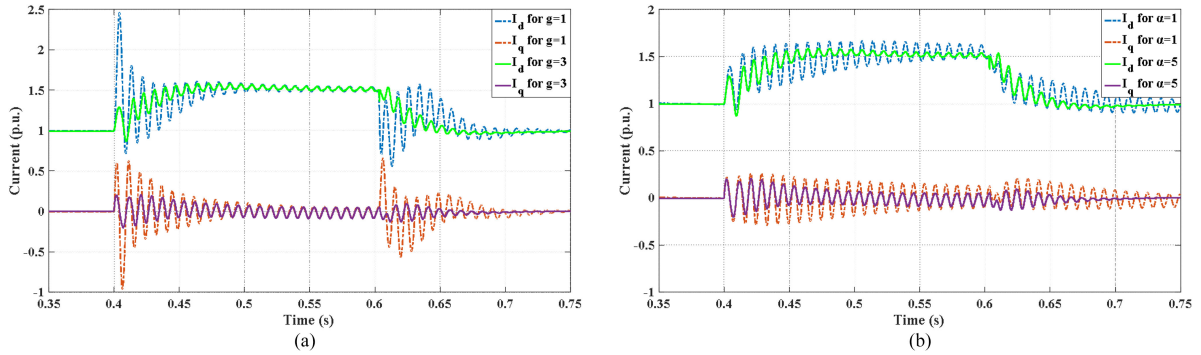


Fig. 20. Positive sequence current in  $dq^+$  frame for BPSC strategy with (a) different  $g$  values and, (b) different  $\alpha$  values.

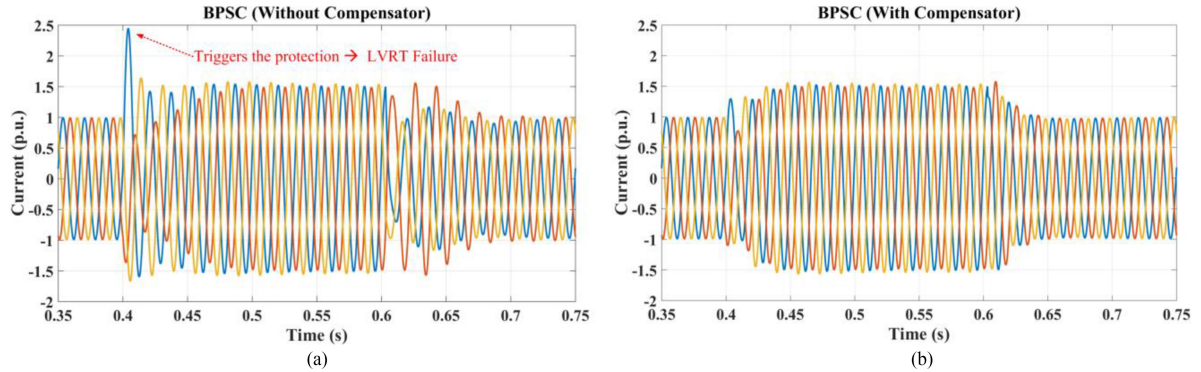


Fig. 21. Three-phase current results in BPSC strategy using: (a) CC without applying the compensator (b) CC with applying the improved compensator.

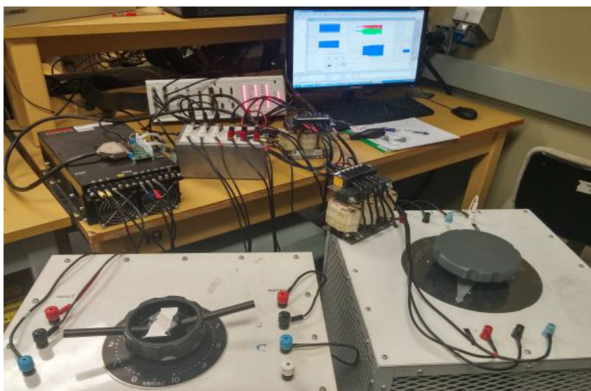


Fig. 22. Experimental test setup.

section, this fact is also illustrated using the experimental test system. Fig. 24(a) shows the results for the BPSC strategy. It is observed that for lower  $K_{p2}$  (starts from  $K_{p2} = 1$ ) the system remains stable. Then,  $K_{p2}$  is increased gradually, and it is illustrated that the system has lost the stability for  $K_{p2} > 25$ .

### C. System Performance Under Different SCRs

As presented earlier, the system SCR should be considered in designing the system controllers. The effect of SCR on selecting PLL parameters is studied using the small-signal model. To validate the results, two different system SCRs are implemented in this section, and the previous tests of Section B are repeated. The results are presented in Fig. 24. It is again observed that in lower SCRs, the PLL gain selection is more restricted, and  $K_{p2}$

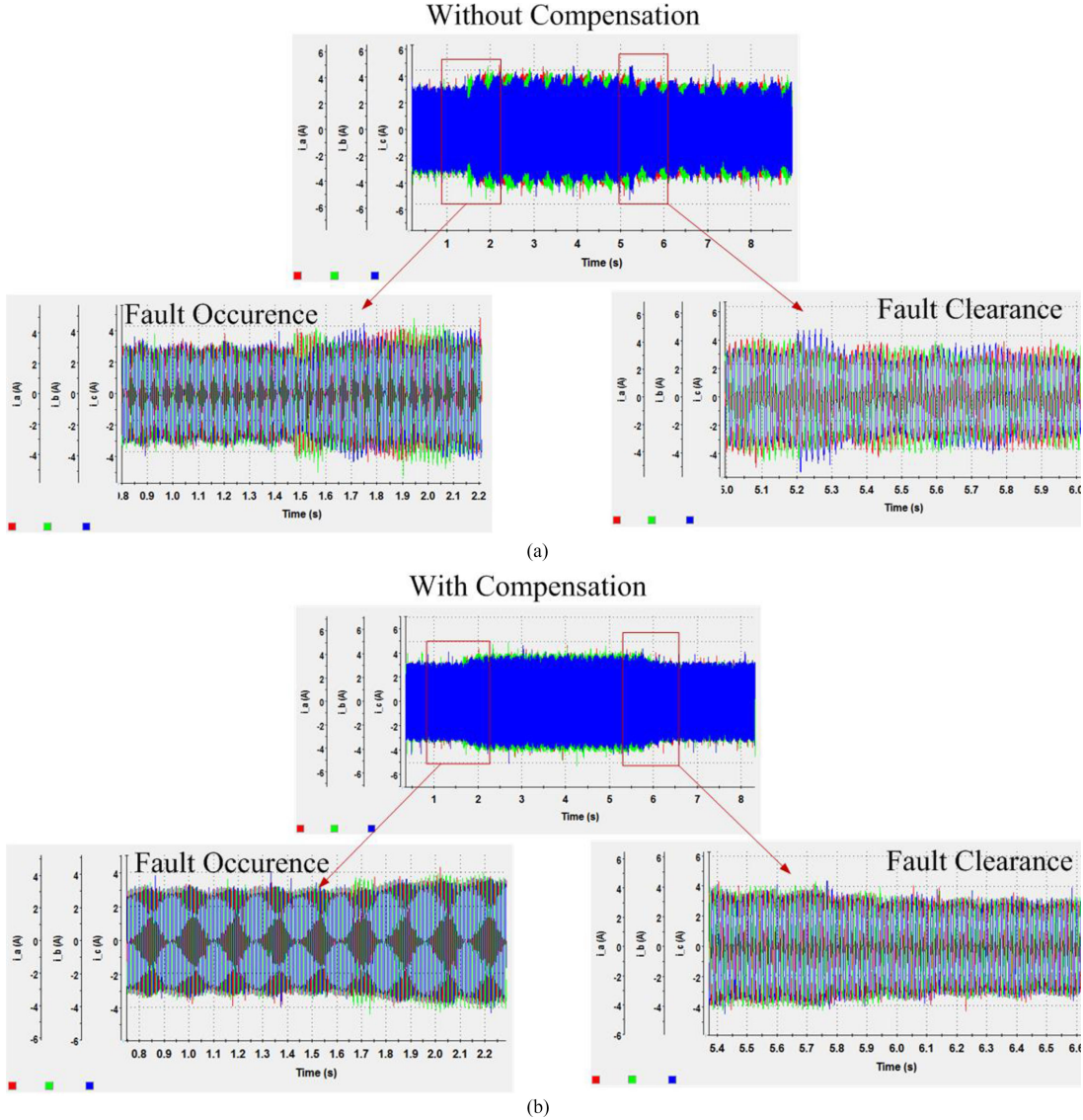


Fig. 23. Effect of applying the proposed compensation method on BPSC behavior for fault transients in experimental setup: (a) without compensation, and (b) with the proposed compensation method.

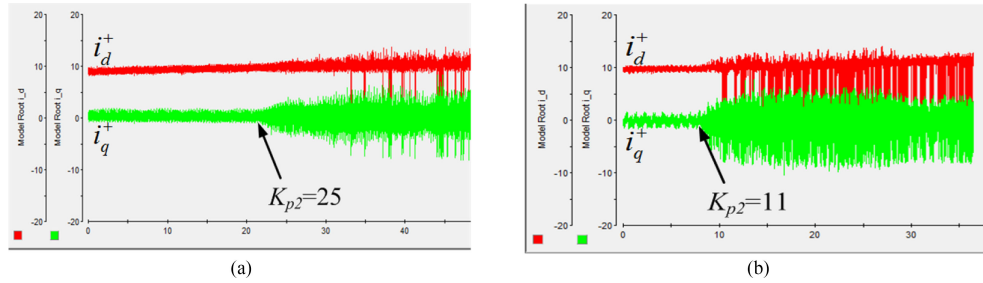


Fig. 24. Effect of increasing  $K_{p2}$  on experimental test system stability under (a) higher SCR and (b) lower SCR.

has a lower threshold to maintain the system stability. For example, in this case, the system remains stable until  $K_{p2} = 25$  for higher SCR; but, for a system with lower SCR, the system loses its stability for  $K_{p2} > 11$ . Therefore, in designing the system controllers, the power system strength effects on selecting the PLL parameters should be properly considered.

## VII. CONCLUSION

Detailed small-signal model and analysis of the dynamics of a grid-connected VSC equipped with the recently developed balanced positive-sequence control and positive-negative-sequence control methods to support the grid under unbalanced conditions have been presented in this paper. The impacts of

the SCR, angle of the ac system impedance, and phase-locked-loop parameters on the transient behavior of the VSC have been thoroughly studied and characterized. Furthermore, to improve the dynamic performance of grid-connected VSCs, a simple yet effective current-control-based compensator has been developed to mitigate possible instabilities associated with the low-voltage operation. Comparative simulation and experimental results have been used to validate the theoretical analysis and the effectiveness of the proposed compensation scheme. The study has revealed the following:

- 1) For strong grids ( $SCR > 3$ ), the BPSC is the best choice because it has balanced and sinusoidal current during the fault. Also, it exhibits the lowest  $I_{max}$  value.
- 2) In a weak grid with low  $X/R$  ratio, the PNSC strategy is a superior choice as compared to the BPSC because its damping ratio reveals minor changes and stays above zero.
- 3) In systems with more sensitive protection devices, the BPSC strategy should be adopted because of its considerably lower  $I_{max}$  value.

## APPENDIX

### A. Derivation of the BPSC Strategy Small-Signal Equations

The equations of the BPSC reference currents using (12)–(14) are

$$\begin{aligned} i_d^{*+} &= \frac{\frac{2}{3}P_{ref}V_{pd}^+}{(V_{pd}^{+2} + V_{pq}^{+2})} + \frac{\frac{2}{3}Q_{ref}V_{pq}^+}{(V_{pd}^{+2} + V_{pq}^{+2})} \\ i_q^{*+} &= \frac{\frac{2}{3}P_{ref}V_{pq}^+}{(V_{pd}^{+2} + V_{pq}^{+2})} - \frac{\frac{2}{3}Q_{ref}V_{pd}^+}{(V_{pd}^{+2} + V_{pq}^{+2})}. \end{aligned}$$

The linearized BPSC reference currents, i.e.,  $\Delta i_d^{*+}$  and  $\Delta i_q^{*+}$  are obtained as follows:

$$\begin{aligned} \Delta i_d^{*+} &= \frac{2}{3}P_{ref} \left[ \frac{-m_2}{den} \Delta V_{pd}^+ + \frac{m_1}{den} \Delta V_{pq}^+ \right] \\ &\quad + \frac{2}{3}Q_{ref} \left[ \frac{m_1}{den} \Delta V_{pd}^+ + \frac{m_2}{den} \Delta V_{pq}^+ \right] \\ \Delta i_q^{*+} &= \frac{2}{3}P^* \left[ \frac{m_1}{den} \Delta V_d^+ + \frac{m_2}{den} \Delta V_q^+ \right] \\ &\quad - \frac{2}{3}Q^* \left[ \frac{-m_2}{den} \Delta V_d^+ + \frac{m_1}{den} \Delta V_q^+ \right]. \end{aligned}$$

In which

$$m_1 = -2 V_{pd-ss}^+ V_{pq-ss}^+, \quad m_2 = V_{pd-ss}^{+2} - V_{pq-ss}^{+2},$$

$$den = \left( V_{pd-ss}^{+2} + V_{pq-ss}^{+2} \right)^2$$

Subscripts  $ss$  denote the steady-state value.

### B. Derivation of the PNSC Strategy Small-Signal Equations

The equations of the PNSC reference currents using (16)–(18) are

$$\begin{aligned} i_d^{*+} &= \frac{\frac{2}{3}P_{ref}V_{pd}^+}{|V_p^+|^2 - |V_p^-|^2} - \frac{\frac{2}{3}Q_{ref}V_{pq}^+}{|V_p^+|^2 - |V_p^-|^2} \\ i_d^{*-} &= \frac{-\frac{2}{3}P_{ref}V_{pd}^-}{|V_p^+|^2 - |V_p^-|^2} - \frac{\frac{2}{3}Q_{ref}V_{pq}^-}{|V_p^+|^2 - |V_p^-|^2} \\ i_q^{*+} &= \frac{-\frac{2}{3}P_{ref}V_{pq}^+}{|V_p^+|^2 - |V_p^-|^2} + \frac{\frac{2}{3}Q_{ref}V_{pd}^+}{|V_p^+|^2 - |V_p^-|^2} \\ i_q^{*-} &= \frac{-\frac{2}{3}P_{ref}V_{pq}^-}{|V_p^+|^2 - |V_p^-|^2} + \frac{\frac{2}{3}Q_{ref}V_{pd}^-}{|V_p^+|^2 - |V_p^-|^2}. \end{aligned}$$

The linearized PNSC reference currents, i.e.,  $\Delta i_d^{*+}$ ,  $\Delta i_q^{*+}$ ,  $\Delta i_d^{*-}$ , and  $\Delta i_q^{*-}$  are obtained as follows:

$$\begin{aligned} \Delta i_d^{*+} &= \frac{2}{3}P_{ref} (f_{1-v_{pd}^+} \cdot \Delta v_{pd}^+ + f_{1-v_{pq}^+} \cdot \Delta v_{pq}^+ \\ &\quad + f_{1-v_{pd}^-} \cdot \Delta v_{pd}^- + f_{1-v_{pq}^-} \cdot \Delta v_{pq}^-) \\ &\quad - \frac{2}{3}Q_{ref} (f_{2-v_{pd}^+} \cdot \Delta v_{pd}^+ + f_{2-v_{pq}^+} \cdot \Delta v_{pq}^+ \\ &\quad + f_{2-v_{pd}^-} \cdot \Delta v_{pd}^- + f_{2-v_{pq}^-} \cdot \Delta v_{pq}^-) \\ \Delta i_d^{*-} &= \frac{2}{3}P_{ref} (f_{1-v_{pd}^+} \cdot \Delta v_{pd}^+ + f_{1-v_{pq}^+} \cdot \Delta v_{pq}^+ \\ &\quad + f_{1-v_{pd}^-} \cdot \Delta v_{pd}^- + f_{1-v_{pq}^-} \cdot \Delta v_{pq}^-) \\ &\quad - \frac{2}{3}Q_{ref} (f_{2-v_{pd}^+} \cdot \Delta v_{pd}^+ + f_{2-v_{pq}^+} \cdot \Delta v_{pq}^+ \\ &\quad + f_{2-v_{pd}^-} \cdot \Delta v_{pd}^- + f_{2-v_{pq}^-} \cdot \Delta v_{pq}^-) \\ \Delta i_q^{*+} &= -\frac{2}{3}P_{ref} (f_{5-v_{pd}^+} \cdot \Delta v_{pd}^+ + f_{5-v_{pq}^+} \cdot \Delta v_{pq}^+ \\ &\quad + f_{5-v_{pd}^-} \cdot \Delta v_{pd}^- + f_{5-v_{pq}^-} \cdot \Delta v_{pq}^-) \\ &\quad - \frac{2}{3}Q_{ref} (f_{6-v_{pd}^+} \cdot \Delta v_{pd}^+ + f_{6-v_{pq}^+} \cdot \Delta v_{pq}^+ \\ &\quad + f_{6-v_{pd}^-} \cdot \Delta v_{pd}^- + f_{6-v_{pq}^-} \cdot \Delta v_{pq}^-) \\ \Delta i_q^{*-} &= -\frac{2}{3}P_{ref} (f_{6-v_{pd}^+} \cdot \Delta v_{pd}^+ + f_{6-v_{pq}^+} \cdot \Delta v_{pq}^+ \\ &\quad + f_{6-v_{pd}^-} \cdot \Delta v_{pd}^- + f_{6-v_{pq}^-} \cdot \Delta v_{pq}^-) \\ &\quad + \frac{2}{3}Q_{ref} (f_{5-v_{pd}^+} \cdot \Delta v_{pd}^+ + f_{5-v_{pq}^+} \cdot \Delta v_{pq}^+ \\ &\quad + f_{5-v_{pd}^-} \cdot \Delta v_{pd}^- + f_{5-v_{pq}^-} \cdot \Delta v_{pq}^-). \end{aligned}$$

In which subscripts  $ss$  denote the steady-state value and  $f_x$  coefficients are given below:

$$\begin{aligned} den &= \left( V_{pd-ss}^+ + V_{pq-ss}^+ \right)^2 + \left( V_{pd-ss}^- + V_{pq-ss}^- \right)^2 \\ f_{1-v_p^+} &= \frac{den - 2.V_{pd-ss}^+}{den^2}, \quad f_{1-v_p^-} = \frac{-2.V_{pq-ss}^+ \cdot V_{pd-ss}^+}{den^2} \\ f_{1-v_p^-} &= \frac{2.V_{pd-ss}^- \cdot V_{pd-ss}^+}{den^2}, \quad f_{1-v_p^+} = \frac{2.V_{pq-ss}^- \cdot V_{pd-ss}^+}{den^2} \\ f_{2-v_p^+} &= \frac{-2.V_{pd-ss}^+ \cdot V_{pq-ss}^+}{den^2}, \quad f_{2-v_p^-} = \frac{den - 2.V_{pq-ss}^+}{den^2} \\ f_{2-v_p^-} &= \frac{2.V_{pd-ss}^- \cdot V_{pq-ss}^+}{den^2}, \quad f_{2-v_p^+} = \frac{2.V_{pq-ss}^- \cdot V_{pq-ss}^+}{den^2} \\ f_{5-v_p^+} &= \frac{-2.V_{pd-ss}^+ \cdot V_{pd-ss}^-}{den^2}, \quad f_{5-v_p^-} = \frac{-2.V_{pq-ss}^+ \cdot V_{pd-ss}^-}{den^2} \\ f_{5-v_p^-} &= \frac{den + 2.V_{pd-ss}^-}{den^2}, \quad f_{5-v_p^+} = \frac{2.V_{pq-ss}^- \cdot V_{pd-ss}^-}{den^2} \\ f_{6-v_p^+} &= \frac{-2.V_{pd-ss}^+ \cdot V_{pq-ss}^-}{den^2}, \quad f_{6-v_p^-} = \frac{-2.V_{pq-ss}^+ \cdot V_{pq-ss}^-}{den^2} \\ f_{6-v_p^-} &= \frac{2.V_{pd-ss}^- \cdot V_{pq-ss}^-}{den^2}, \quad f_{6-v_p^+} = \frac{den + 2.V_{pq-ss}^-}{den^2} \end{aligned}$$

## REFERENCES

- [1] J. Sosa, M. Castilla, J. Miret, J. Matas, and Y. Al-Turki, "Control strategy to maximize the power capability of PV three-phase inverters during voltage sags," *IEEE Trans. Power Electron.*, vol. 31, no. 4, pp. 3314–3323, Apr. 2016.
- [2] Q. Huang, X. Zou, D. Zhu, and Y. Kang, "Scaled current tracking control for doubly fed induction generator to ride-through serious grid faults," *IEEE Trans. Power Electron.*, vol. 31, no. 3, pp. 2150–2165, May 2016, doi: 10.1109/TPEL.2015.2429153.
- [3] D. Shin, K.-J. Lee, J.-P. Lee, D.-W. Yoo, and H.-J. Kim, "Implementation of fault ride-through techniques of grid-connected inverter for distributed energy resources with adaptive low-pass notch PLL," *IEEE Trans. Power Electron.*, vol. 30, no. 5, pp. 2859–2871, May 2015.
- [4] R. H. Salim and R. A. Ramos, "Analyzing the effect of the type of terminal voltage feedback on the small signal dynamic performance of synchronous generators," in *Proc. 2010 IREP Symp. Bulk Power Syst. Dyn. Control—VIII*, Aug. 2010, pp. 1–7.
- [5] R. H. Salim, R. A. Ramos, and N. G. Bretas, "Analysis of the small signal dynamic performance of synchronous generators under unbalanced operating conditions," in *Proc. IEEE Power Energy Soc. General Meeting*, Jul. 2010, pp. 1–6.
- [6] Ö. Göksu, R. Teodorescu, C. L. Bak, F. Iov, and P. C. Kjær, "Instability of wind turbine converters during current injection to low voltage grid faults and pll frequency based stability solution," *IEEE Trans. Power Syst.*, vol. 29, no. 4, pp. 1683–1691, Jul. 2014.
- [7] P. Rodriguez, A. V. Timbus, R. Teodorescu, M. Liserre, and F. Blaabjerg, "Flexible active power control of distributed power generation systems during grid faults," *IEEE Trans. Ind. Electron.*, vol. 54, no. 5, pp. 2583–2592, Oct. 2007.
- [8] S. Golestan, J. M. Guerrero, A. Vidal, A. G. Yepes, J. Doval-Gandoy, and F.D. Freijedo, "Small-signal modeling, stability analysis, and design optimization of single-phase delay-based PLLs," *IEEE Trans. Power Electron.*, vol. 31, no. 5, pp. 3517–3527, May 2016, doi: 10.1109/TPEL.2015.2462082.
- [9] R. H. Salim and R. A. Ramos, "A model-based approach for small-signal stability assessment of unbalanced power systems," *IEEE Trans. Power Syst.*, vol. 27, no. 4, pp. 2006–2014, Nov. 2012.
- [10] A. Kahrobaeian and Y. A. R. I. Mohamed, "Analysis and mitigation of low-frequency instabilities in autonomous medium-voltage converter-based microgrids with dynamic loads," *IEEE Trans. Ind. Electron.*, vol. 61, no. 4, pp. 1643–1658, Apr. 2014.
- [11] Wen Bo, D. Boroyevich, R. Burgos, P. Mattavelli, and Z. Shen, "Small-signal stability analysis of three-phase AC systems in the presence of constant power loads based on measured d-q frame impedances," *IEEE Trans. Power Electron.*, vol. 30, no. 10, pp. 5952–5963, Oct. 2015.
- [12] P. W. Sauer and M. A. Pai, *Power System Dynamics and Stability*. Englewood Cliffs, NJ, USA: Prentice-Hall, 1998.
- [13] C. N. Rowe, T. J. Summers, R. E. Betz, D. J. Cornforth, and T. G. Moore, "Arctan power–frequency droop for improved microgrid stability," *IEEE Trans. Power Electron.*, vol. 28, no. 8, pp. 3747–3759, Aug. 2013.
- [14] S.-F. Chou, C.-T. Lee, H.-C. Ko, and P.-T. Cheng, "A low-voltage ride-through method with transformer flux compensation capability of renewable power grid-side converters," *IEEE Trans. Power Electron.*, vol. 29, no. 4, pp. 1710–1719, Apr. 2014.
- [15] M. Ebrahimi, S. Khajehoddin, and M. K. Ghartemani, "Fast and robust single-phase DQ current controller for smart inverter applications," *IEEE Trans. Power Electron.*, vol. 31, no. 5, pp. 3968–3976, May 2016.
- [16] T. Yi, Q. Zian, F. Blaabjerg, and L. P. Chiang, "A dual voltage control strategy for single-phase PWM converters with power decoupling function," *IEEE Trans. Power Electron.*, vol. 30, no. 12, pp. 7060–7071, Dec. 2015.
- [17] D. Dong, B. Wen, P. Mattavelli, D. Boroyevich, and Y. Xue, "Modeling and design of islanding detection using phase-locked loops in three-phase grid-interface power converters," *IEEE J. Emerg. Sel. Topics Power Electron.*, vol. 2, no. 4, pp. 314–323, Dec. 2014.
- [18] L. Xu and Y. Wang, "Dynamic modeling and control of DFIG-based wind turbines under unbalanced network conditions," *IEEE Trans. Power Syst.*, vol. 22, no. 1, pp. 314–323, Feb. 2007.
- [19] M. M. Shabestary, "A comparative analytical study on low-voltage ride-through reference-current-generation (LVRT-RCG) strategies in converter-interfaced der units," M.S. thesis, ECE Dept., Univ. Alberta, Edmonton, AB, Canada, 2014.
- [20] R. Teodorescu, M. Liserre, and P. Rodriguez, "Control of grid converters under grid faults" in *Grid Converters for Photovoltaic and Wind Power Systems*. Hoboken, NJ, USA: Wiley, Feb. 2011.
- [21] J. Z. Zhou, H. Ding, S. Fan, Y. Zhang, and A. M. Gole, "Impact of short-circuit ratio and phase-locked-loop parameters on the small-signal behavior of a VSC-HVDC converter," *IEEE Trans. Power Del.*, vol. 29, no. 5, pp. 2287–2296, Oct. 2014.
- [22] *IEEE Guide for Planning DC Links Terminating at AC Locations Having Low Short-Circuit Capacities*, IEEE Std 1204-1997, 1997.
- [23] A. Yazdani and R. Iravani, *Voltage-Sourced Converters in Power Systems: Modeling, Control, and Applications*. Hoboken, NJ, USA: Wiley, 2010.
- [24] L. Harnefors, M. Bongiorno, and S. Lundberg, "Input-admittance calculation and shaping for controlled voltage-source converters," *IEEE Trans. Ind. Electron.*, vol. 54, no. 6, pp. 3323–3334, Dec. 2007.



**Shahed Mortazavian** (S'15) received the B.Sc. degree from the Isfahan University of Technology, Isfahan, Iran, and the M.Sc. degree from the Amirkabir University of Technology, Tehran, Iran, both in electrical engineering, in 2007 and 2013, respectively. She is currently working toward the Ph.D. degree in electrical and computer engineering at the University of Alberta, Edmonton, AB, Canada.

Her research interests include dynamics and control of power converters, power systems and microgrids stability, renewable generation, and fault diagnosis and condition monitoring in power systems.



**Masoud M. Shabestary** (S'14) received the B.Sc. degree in electrical engineering from Amirkabir University of Technology (Tehran Polytechnic), Tehran, Iran, in 2011 and the M.Sc. degree in energy systems from the University of Alberta, Edmonton, AB, Canada, in 2015. He is currently working toward the Ph.D. degree in electrical engineering at the University of Alberta.

From 2011 to 2013, he served as a Research Assistant at the FACTS laboratory, Amirkabir University of Technology, Tehran. His research interests include renewable energy and distributed generation units, their analysis, control, and protection, and application of power converters in smart hybrid ac/dc microgrids.



**Yasser Abdel-Rady I. Mohamed** (M'06–SM'011) was born in Cairo, Egypt, on November 25, 1977. He received the B.Sc.Hons. and M.Sc. degrees in electrical engineering from Ain Shams University, Cairo, in 2000 and 2004, respectively, and the Ph.D. degree in electrical engineering from the University of Waterloo, Waterloo, ON, Canada, in 2008.

He is currently with the Department of Electrical and Computer Engineering, University of Alberta, AB, Canada, as a Professor. His research interests include dynamics and controls of power converters; grid integration of distributed generation and renewable resources, microgrids, modeling, analysis, and control of smart grids; and electric machines and motor drives.

Dr. Mohamed is an Associate Editor of the IEEE TRANSACTIONS ON INDUSTRIAL ELECTRONICS and IEEE TRANSACTIONS ON POWER ELECTRONICS, and an Editor of the IEEE TRANSACTIONS ON POWER SYSTEMS and IEEE TRANSACTIONS ON SMART GRID. He is a registered Professional Engineer in the Province of Alberta.